Assessing the progression of wind turbine energy yield losses due to blade erosion by resolving damage geometries from lab tests and field observations

Alessio Castorrini [a,b], Andrea Ortolani [a], M. Sergio Campobasso [a,*]

[a] *Lancaster University, School of Engineering, Lancaster LA1 4YW, United Kingdom*
[b] *Sapienza University of Rome, Department of Mechanical and Aerospace Engineering, Via Eudossiana 18, 00184 Rome, Italy*

ARTICLE INFO

ABSTRACT

Predicting losses of wind turbine energy yield due to blade leading edge erosion is a major challenge, hindering blade predictive maintenance, and preventing further cost of energy reductions. Using jointly laser scans of operational offshore turbines, photographs of eroded leading edge samples from swirling arm rain erosion tests and validated simulation methods, this study estimates the growth of energy yield losses as erosion progresses from small-scale distributed roughness to severe damage of the leading edge. A multi-fidelity analysis is employed, combining high-fidelity computational fluid dynamics and blade element momentum theory. Erosion-induced aerodynamic performance losses are analyzed with a scale separation approach, modeling the effects of low-amplitude roughness with generalized rough-wall functions, and capturing the effects of larger geometry alterations by geometrically resolving them. The sensitivity of energy losses to the level of equivalent sand grain roughness, an uncertain parameter of the problem, is analyzed. For a typical North Sea installation site, the loss of energy grows from 0.6%, for moderate modeled roughness, to 2%, for resolved severe erosion. The largest loss at a typical Southern European onshore site is 2.5%. Severe erosion-induced energy losses are found to vary significantly with the damage topography, emphasizing the necessity or resolving larger erosion scales.

1. Introduction

Wind energy is a major player in the clean energy transition, carrying a significant weight for meeting stringent and urgent targets of carbon emission reduction [1]. Onshore wind is already one of the most sustainable renewable energy technologies; a higher levelized cost of energy (LCOE) resulted in an initially slower deployment of offshore wind [2], but fast technological advances in offshore engineering are now lowering offshore wind LCOE, prompting a large scale exploitation of this resource worldwide. Since LCOE decreases as the Annual Energy Production (AEP) of wind farms increases, all sources of AEP losses need to be assessed, and mitigated or removed. One of these losses is that due to blade Leading Edge Erosion (LEE), which reduces turbine power and energy yield due to reduced aerodynamic performance of the blades and the resulting reduction of rotor torque.

The AEP loss due to LEE is difficult to measure, partly because it depends on the detailed geometry of the eroded surface. To date, the actual value of AEP lost to LEE is uncertain, with recently reported estimates for wind farms ranging from 0.5 to 8% [3–7]. The large scatter of the reported AEP losses is partly due to the fact that this quantity depends on the specific geometry of the blade surface perturbation caused by the Leading Edge (LE) material loss. At its onset, erosion increases LE surface roughness, whereas it yields larger alterations of the nominal LE geometry at more advanced stages. The aerodynamic performance loss at these two extremes varies significantly for both level and governing physics.

LEE impairs the aerodynamic performance of the blade airfoils, yielding a reduction of the maximum lift force, an increase of the total drag force at all values of the Angle of Attack (AoA), and a reduction of the stall margin, due to a reduction of the AoA at which stall commences [8–10]. At the initial LEE stages, characterized by small-scale roughness, one has a shift towards the LE of the chordwise position where laminar-to-turbulent transition of the boundary layer (BL) occurs on the airfoil upper side [11,12]. The larger wall shear stress and thickness of turbulent BLs [13] start increasing the total drag and reducing the lift. When roughness reaches levels exceeding a critical roughness height [14], laminarity is completely lost, and BLs are turbulent from their onset at the LE. Furthermore, the roughness elements perturb also the turbulent BL, increasing further the pressure drag at the wall, a phenomenon that intensifies as wall roughness increases.

---

* Corresponding author.
E-mail address: m.s.campobasso@lancaster.ac.uk (M.S. Campobasso).

As erosion progresses and the perturbations of the LE geometry approach or exceed the BL thickness, additional aerodynamic losses occur, which may vary significantly with the specific LEE damage [15]. These phenomena contribute, with strength depending on the erosion severity, to premature separation of the BL on the airfoil upper side at AoAs where the nominal airfoil has a clean flow [7,16,17], with consequent reduction of the lift and further increase of the drag.

Enabling reliable predictions of the AEP loss caused by given LEE damages would provide wind turbine operators with an additional tool to reduce LCOE by optimizing the trade-off of AEP revenue and blade maintenance costs (predictive maintenance). Blade inspection data acquired with remote monitoring of the blade state, for example by using autonomous drone-based inspection technologies [18–21] can be fed into the AEP loss prediction system (ALPS) [5,17,22], which calculates the loss of energy yield due to the observed damage, a key input for the predictive maintenance cost analysis.

Several numerical and experimental approaches have been applied to investigate the aerodynamics and performance implications of LEE. Maniaci et al. [11] modeled LEE and other LE perturbations by means of trip tape and vinyl stickers. Different levels and patterns of roughness were applied on the LE of wind tunnel models of the NACA63$_3$-418 and NREL S814 airfoils. The aerodynamic force coefficients were measured at Reynolds number (Re) of 3.2M. A similar approach was adopted by Kruse et al. [23], who applied sandpaper, zig-zag tapes and 2D LE cavities of constant depth to the wind tunnel model of the NACA63$_3$-418 airfoil, tested at Re = 3M and Re = 5M. Wind tunnel experiments were also conducted using geometrically more complex models of LEE. Gaudern et al. [24] applied to the LE of the wind tunnel airfoil model, an erosion tape profiled using waterjet cutting to replicate irregular erosion patterns observed in field operation. Sareen et al. [25] modeled LEE by removing material from the LE of the wind tunnel model of a DU 96-W-180 airfoil, reproducing random distributions of hemispherical erosion cavities and chordwise grooves at the LE.

Computational Fluid Dynamics (CFD) is also extensively used to assess the detrimental effects of LEE at the high Reynolds numbers of the outboard blade sections of utility-scale turbines. A simple approach to account for the effects of roughness consists of using a distributed wall roughness model applied to the nominal airfoil geometry [26]. This approach may account for the impact of distributed roughness due to moderate erosion on anticipating or suppressing BL transition and increasing surface drag of turbulent BLs. However, this method is inapplicable when the roughness height approaches or exceeds the BL thickness [27,28], which is the case of the large roughness caused by severe LEE. In this circumstance, the geometry of the roughness elements needs to be resolved.

Schramm et al. [29], Campobasso et al. [22] and Papi et al. [30] modeled severe LEE with 2D LE grooves of depth and chordwise extent based on field observations and literature, and assessed their performance impairment with 2D Reynolds-averaged Navier–Stokes (RANS) simulations. Wang et al. [31] used 2D RANS CFD to study the S809 airfoil performance degradation caused by distributed circular erosion pits. Successively, Castorrini et al. [32] and Campobasso et al. [17] investigated LE pitting by means of 3D RANS analyses, geometrically resolving hemispherical LE cavities and including distributed roughness modeling to account for the effect of smaller unresolved roughness scales. Han et al. [3] performed 2D RANS analyses of three geometrically resolved erosion patterns derived from field observations, using a distributed roughness model to account for the impact of unresolved roughness. The study also used the computed force coefficient data of the eroded airfoils in the aero-servo-elastic simulation analysis of a reference wind turbine to determine the AEP losses for selected installation sites, an approach adopted also in [17,22,30].

So far, most CFD investigations into the aerodynamics of eroded wind turbine blades relied on fairly simple representations of LEE geometry. A recent study by Ortolani et al. [15] presented the first assessment of the airfoil performance reduction caused by LEE making

use of the eroded LE geometry from the 3D laser scan of a utility-scale offshore turbine blade. Their RANS simulations adopted a scale separation approach to the analysis of multi-scale roughness, resolving the erosion geometry of the scan and modeling the impact of roughness scales unresolved by the scan with a distributed surface roughness model. Aerodynamic analyses of three blade sections extracted from the scan were preformed to assess the sensitivity of the lift coefficient c_l and the drag coefficient c_d to real LEE. Recently, the impact of resolved LEE on blade aerodynamic performance was also investigated with 3D RANS CFD using the geometry from the scan of the eroded blade of an onshore turbine [33].

The investigations of the present study are partly based on the eroded LE laser scan of [15], and the main objectives of the work are: (a) to assess the progression of power and AEP losses as LEE severity increases using the scale separation CFD analysis of erosion-induced LE roughness, (b) to investigate the dependence of these losses on the resolved erosion geometry, which, in turn, depends also on the structural properties of the LE material, and (c) to investigate the sensitivity of the blade performance degradation and turbine AEP loss to the level of the equivalent sand grain roughness, a parameter affected by uncertainty due to its dependence on the typically unknown geometry of the unresolved roughness scales.

The article structure is as follows. Section 2 presents the simulation codes used by ALPS; Section 3 describes and discusses the selected case study, including the definition of the reference wind turbine, its damaged variants, and a representative offshore and onshore site for the AEP loss analyses. Results and discussions of blade section aerodynamics, turbine power and AEP losses, and turbine loads and control parameters of the considered eroded turbines are provided in Section 4. A summary of the study is provided in Section 5.

2. Methodology

The computation of the AEP losses due to LEE is based on the ALPS technology [5,22]. The input of the ALPS analysis can be subdivided in three main groups. The first group consists of the nominal turbine definition, i.e. rotor radius and hub height, radial profiles of blade chord and twist, blade airfoil geometry and turbine control strategy. These data are defined in Section 3.1. The second data group defines the blade surface alterations due to erosion. The definition of all LE damage variants considered in this study, and the scale separation approach adopted for their analyses are defined and discussed in Sections 3.2 and 3.3. The third data group consists of the wind characteristic of the considered site, i.e. turbulence data, yearly mean wind speed and wind frequency data, and vertical wind shear. These data, for the considered offshore and onshore installation sites, are provided in Section 3.4.

ALPS requires an estimate of the nominal airfoil geometry for two reasons. One is computing the power curve and the AEP of the nominal turbine, with the latter quantity used as reference to calculate the AEP loss of the damaged turbine. The other reason is enabling the parametrization of the erosion geometry, needed for the robustness of the CFD geometry and mesh generation. The parametrization requires computing the erosion-induced surface alterations relative to the nominal geometry, as explained in Section 3.2. Once the geometry of the nominal airfoils and that of its perturbed variants are available, the airfoil force coefficients are computed. These data, in the form of curves providing lift coefficient c_l and drag coefficient c_d as functions of the AoA α are part of the input of the wind turbine performance analysis module, presently using the Blade Element Momentum Theory (BEMT) for rotor aerodynamics (see Section 2.1). The ALPS estimate of the curves $c_l(\alpha)$ and $c_d(\alpha)$ is based on RANS CFD, and the adopted set-up is summarized in Section 2.2. ALPS can also use artificial neural networks for the rapid estimate of the force coefficients of the eroded blade sections [5,22].

The AEP loss of the damaged turbine is obtained by first computing the power curve of the nominal and damaged turbines, and then calculating the AEP of the two turbines at the given site. The AEP loss is the difference of these two values.

2.1. Wind turbine analysis module

The turbine power curve is computed using OpenFAST [34], a multi-body aero-hydro-servo-elastic wind turbine analysis code. Rotor aerodynamics is handled by the BEMT library AeroDyn - version 15 [35], which uses semiempirical corrections, such as the tip and root Prandtl correction [36], Minnema/Pierce variant of Beddoes-Leishman dynamic stall model [37], and the skewed-wake correction model of Pitt-Peters [35] to account for complex rotor aerodynamics features not handled by the baseline BEMT formulation.

In all OpenFAST simulations of this study, blades and tower are assumed rigid, and the foundation is fixed. The turbine uses rotor speed control from cut-in to rated wind speed, and blade pitch control from rated to cut-out wind speed. The analyses use turbulent wind conditions. Each point of the power curve refers to a particular wind speed V at hub height, and is obtained by time-averaging the output power of a 10-min time-dependent simulation of the NREL 5 MW reference turbine [38], the baseline turbine of this study. The velocity V ranges from 4 (close to cut-in) to 25 m/s (cut-out), with step of 1 m/s. Between 11 and 12 m/s a smaller step of 0.2 m/s is used to resolve the knee of the power curve around rated wind speed, where the power control transitions from the variable-speed to the constant-speed and variable-pitch regime. Each analysis simulates 10.5 min of operation, with time-step of 0.01 s, and the first 30 s of the output are excluded from the averaging process.

For each mean wind speed, the 10.5-min time series of the three wind velocity components are generated with the stochastic wind generator TurbSim [39] on a square domain of side 145 m, containing the projection of the rotor swept area, and discretized with 30 intervals in both directions. The spatial and temporal turbulent fluctuations are generated with the Kaimal spectral method [40], as recommended in the IEC61400 Standard. The exponent of the power law for the vertical wind shear, and the turbulence intensity (TI) for each mean wind speed refer to specific offshore and onshore sites defined in Section 3.4.

2.2. CFD method

The force coefficients c_l and c_d of the blade sections are computed with 2D aerodynamic simulations, using ANSYS FLUENT version 19 - R3 [41]. In all simulations, the flow field is considered 2D, incompressible, single–phase and turbulent. The RANS equations are solved in conjunction with Menter's two-equation $k - \omega$ shear stress transport (SST) model [42] for the turbulence closure. For the nominal airfoil geometries, laminar-to-turbulent transition of the BLs is simulated by using the Langtry-Menter four-equation $\gamma - Re_\theta$ SST transition model [43–45]. The model couples to the two transport equations of the SST model, two additional transport equations, one for the momentum thickness Reynolds number Re_θ and the other for the turbulence intermittency γ. The Kato-Launder turbulence production limiter [46] is also used in transitional BL simulations.

In addition to resolving the LE erosion geometry, the simulations of the damaged airfoils also use a distributed roughness model to account for the effects of erosion scales unresolved by the scan. The distributed roughness is included in the $\gamma - Re_\theta$ SST transition model through a modification of the Re_θ field equation to account for the increase of the BL momentum thickness due to the unresolved roughness. The correction function depends on the geometric height K of the modeled distributed roughness [17].

Near rough wall boundaries, FLUENT applies an automatic wall treatment based on a rough wall function. This enables determining the wall shear stress τ_w and the friction velocity $u_\tau = (\tau_w/\rho)^{1/2}$ using an analytic expression. This expression depends on the nondimensionalized wall distance $y^+ = y_w u_\tau/\nu$ of the first cell center off the wall from the wall itself, the nondimensionalized velocity component parallel to the wall $u^+ = u_w/u_\tau$ at y_w, and the nondimensionalized equivalent sand grain roughness $K_s^+ = K_s u_\tau/\nu$. Here, y_w, K_s, u_w and ν are, respectively,

the dimensional distance of the first cell center off the wall from the wall itself, the equivalent sand grain roughness, the dimensional velocity parallel to the wall at y_w, and the kinematic viscosity. The law of the rough wall used to compute u_τ is a generalization of the smooth wall logarithmic law [47], introducing an offset Δu^+ depending on K_s^+ [13]. Furthermore, the local y^+ value is automatically increased by $K_s^+/2$ when $K_s > y_w$ to avoid a singularity in the calculation of u_τ [17,41]. A similar approach is used for calculating the specific turbulent dissipation rate ω at the rough wall.

All steady-state CFD simulations use the COUPLED solver, which integrates in a strongly coupled fashion the continuity and momentum equations, and in a loosely coupled manner all other transport equations. A second order space discretization is used for all conservation laws.

As in previous works [17,22], the constant a_1 in the expression of the SST eddy viscosity is changed from 0.31 to 0.28 in all NACA63$_3$-618 airfoil analyses below, to improve the agreement between computed and measured force coefficients of this airfoil [15].

The aerodynamic force coefficients are computed over the interval $-8° \leq \alpha \leq 14°$ with a step of 2°. Time-dependent simulations, based on the loosely coupled SIMPLE integration, are used for the two LE damages consisting of chordwise grooves, defined in Section 3.2. This is needed to cope with the aerodynamic instabilities at the lowest and highest AoAs. Each simulation is carried on for 3000 time-steps, performing 25 sub-iterations per time-step. The time-step is obtained by dividing in 35 intervals the time taken by the air flow to cover one chord length. The far field TI and turbulent length scale in all NACA63$_3$-618 airfoil simulations below are set to 0.1% and 0.2 chords, respectively. All other simulations converge using the pseudo-transient method of the steady solver, achieving good convergence levels using 4000 iterations.

For each airfoil geometry, the CFD analysis is performed at Reynolds numbers of 6.5M, 8.2M and 11.5M, accounting for the variability of this parameter with the rotor speed. The three values are those of the outboard part of the blade at wind speeds of 3 m/s (cut-in speed), 7 m/s and 11.4 m/s (rated speed), respectively. The aerodynamic force coefficient curves for V between 3 and 7 m/s are obtained by interpolating between those computed for Re = 6.5M and Re = 8.2M, whereas, for V between 7 and 11.4 m/s, the curves are interpolated between those for Re = 8.2M and Re = 11.5M. Above rated wind speed, the curves for Re = 11.5M are used. For each Reynolds number, the force coefficient curves from $-180°$ to $180°$, needed by the AeroDyn BEMT library embedded in OpenFAST, are obtained by extrapolating the CFD-based curves using Viterna's method [48], implemented in the NREL Airfoilprep tool [49] used in this work.

All CFD and OpenFAST computations have been performed on the Lancaster University HEC cluster [50], using the message passing interface (MPI) libraries for the CFD simulations, and running concurrently multiple OpenFAST simulations.

3. Case study

3.1. Wind turbine model

The laser scan of the eroded blade of a utility-scale offshore turbine used in this study covers the front part of the blade outer portion, starting from the LE. To complete the blade geometry in the chordwise direction, the NACA63$_3$-618 airfoil has been found to be the airfoil best matching the scan. Moreover, the blade of the NREL 5 MW reference turbine has similar geometric characteristics as that of the offshore turbine from which the scan has been taken. Therefore, a modified version of the NREL 5 MW turbine is taken as the reference turbine of this investigation. The blade of the modified reference turbine is obtained by replacing the NACA64$_3$-618 airfoil, the original airfoil of this turbine, used from about 70% rotor radius to the blade tip, with the NACA63$_3$-618 airfoil. The geometry of the blade elements of the eroded
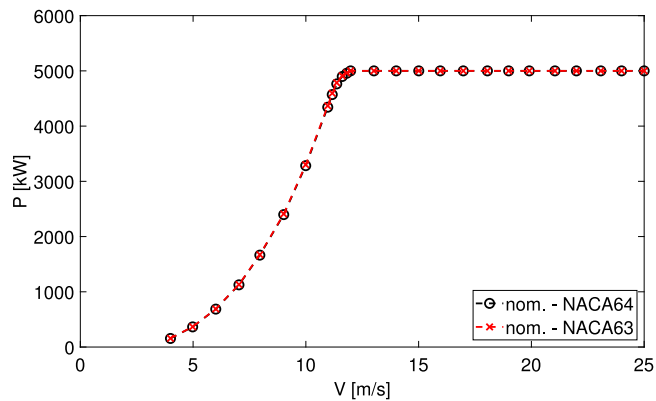
Fig. 1. Power curves of baseline and modified versions of NREL 5 MW wind turbine.

Fig. 2. Portion of 3D blade geometry reconstructed from laser scan.

blade are defined using data of the scan, as described in Section 3.2. The rest of the blade design is that of the original NREL 5 MW turbine.

Fig. 1 compares the power curve of the original NREL 5 MW turbine, and that of the modified reference turbine. The $c_l(\alpha)$ and $c_d(\alpha)$ curves of both the NACA64$_3$-618 and the NACA63$_3$-618 airfoils have been computed using the CFD set-up defined in Section 2.2 at Re = 6M. The comparison shows negligible differences between the two power curves, highlighting that the considered alteration does not affect the turbine performance significantly, enabling to use all other geometry parameters and the control laws of the NREL 5 MW turbine for the reference turbine of this study.

3.2. Resolved leading edge erosion

The definition of part of the LEE geometries used in this study is based on a 'snapshot' of the eroded LE of an offshore utility-scale wind turbine blade available from a 3D laser scan. In previous studies, ALPS was used to study the AEP loss due to geometrically simpler LEE geometries, corresponding to specific erosion stages. These geometries included hemispherical erosion cavities, often observed at the initial stages of erosion [5,17], and chordwise grooves corresponding to severe erosion stages [5,22]. Assessing the progression of AEP losses as erosion progresses requires consideration of intermediate erosion stages, which may be characterized by higher geometric complexity. To estimate AEP losses at different erosion levels, the damage geometries considered herein include both geometries generated directly from the scan, and parametrized LE chordwise grooves.

The 2D geometries of the damaged blade sections for the CFD analyses are generated from the triangulated surface reconstruction of the damaged LE given by the scan. This surface is sliced in the chordwise direction with each slice providing a polyline of the eroded LE. A total of 2369 slices is extracted. For each slice, the chordwise portions of the polyline without erosion are used as a reference to fit the NACA63$_3$-618 profile to the eroded LE, a process yielding the chord of the airfoil and, thus, completing the section geometry until the trailing edge. Then, the erosion displacement $h(s)$, i.e. the distance between the eroded and the nominal LE normal to the nominal airfoil is computed along the curvilinear coordinate s on the nominal LE. The function $h(s)$ provides a local measure of the material loss caused by erosion. Finally, $h(s)$ is Fourier-transformed and reconstructed with between 700 to 1200 harmonics to obtain an analytical definition of the eroded geometry, improving the robustness of grid generation. Fig. 2 shows a CAD reconstruction of the eroded LE using the processed slides at about 93% rotor radius.

The 2D erosion geometry data extracted from the scan are used to generate four plausible time-consecutive LEE states, an abstraction enabled by the rich variability of the damage geometry along the span. A mild, mean, severe and critical damage are applied to the outer 30%
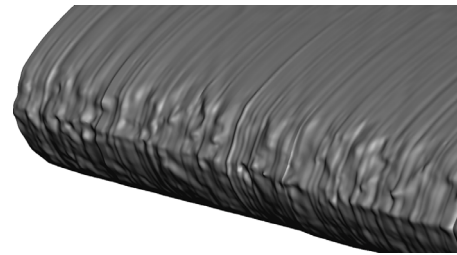
of the blade length, a blade region harvesting a large amount of wind power and more severely hit by erosion, due to the high relative impact speed between blade and rain droplets or other particles. Erosion data were not available at lower radii, but this shortfall is deemed to have a negligible impact on this study, for the reasons above. To reduce the computational cost of the BEMT analyses, each of the four blade models is defined by ten blade strips of equal radial length, and the target level of erosion severity is met by selecting the airfoil geometry of these strips as explained below.

First, the $c_l(\alpha)$ and $c_d(\alpha)$ curves of all 2369 airfoils are calculated. This was done in [15], for Re = 9M and $K = K_s = 0$. Then, one introduces the parameter ε_{RMS}, the root-mean-square of the difference of aerodynamic efficiency $\varepsilon = c_l/c_d$ of damaged and nominal sections. The parameter is computed for a typical range of AoA during operation, here $2° \le \alpha \le 10°$. Therefore,

$$\varepsilon_{RMS} = \sqrt{\sum_{i=1}^{5} \frac{1}{5} \left(\left.\frac{c_l(\alpha_i)}{c_d(\alpha_i)}\right|_{nom.} - \left.\frac{c_l(\alpha_i)}{c_d(\alpha_i)}\right|_{dam.} \right)^2}, \quad \text{with} \quad \alpha_i = 2° + (i-1) \cdot 2°$$

(1)

Fig. 3 plots with black dots the values of ε_{RMS} of the 2369 sections, with each value reported at the radial position of the airfoil it refers to. The dashed vertical lines mark the border between adjacent blade strips. For each strip, the continuous red line is the mean value of ε_{RMS} of the airfoils in the strip. The airfoil for the blade model with mean erosion level is one with the value of ε_{RMS} at the indicated mean level, namely that with the value of ε_{RMS} highlighted with the 'X' symbol.

The mean value of ε_{RMS} divides the airfoils of each strip into two subsets, one with higher, and one with lower ε_{RMS} values. The red dashed and dotted lines denote the median value of the upper and lower subsets, respectively. For each strip, the airfoils for the severe and mild erosion levels are, respectively, those with ε_{RMS} equal to the median of the upper and lower subsets, respectively; their ε_{RMS} is marked by the 'X' symbol. The airfoil with critical damage is one with ε_{RMS} equal to the 95th percentile of the ε_{RMS} set of the strip, indicated with a dash-dotted black line in Fig. 3.

LEE geometry depends on a large number of environmental, turbine control and LE material properties. Two examples of realistic LEE geometries are provided in Fig. 4, which presents photographs of two Leading Edge Protection (LEP) systems after achieving fatigue failure in R&D AS swirling arm rain erosion test facility of the UK Offshore Renewable Energy Catapult. Fig. 4(a) shows the sample LEE geometry observed with an Armour Edge thermoplastic erosion shield (LEP 1), and Fig. 4(b) shows the eroded LE sample geometry of a standard wind industry repair LEP system (LEP 2). One notes that, while the LEE geometry of LEP 1 is relatively smooth, that of LEP 2 features an erosion pattern resembling a series of chordwise grooves.

Parametric models of LEE consisting of LE grooves, with the groove defined by its depth d, and curvilinear lengths s_u and s_l on the airfoil upper and lower sides, respectively, have been used in CFD and wind tunnel investigations of severe LEE [22,25,29,51]. This representation of LEE is a convenient choice in the definition of a digital model
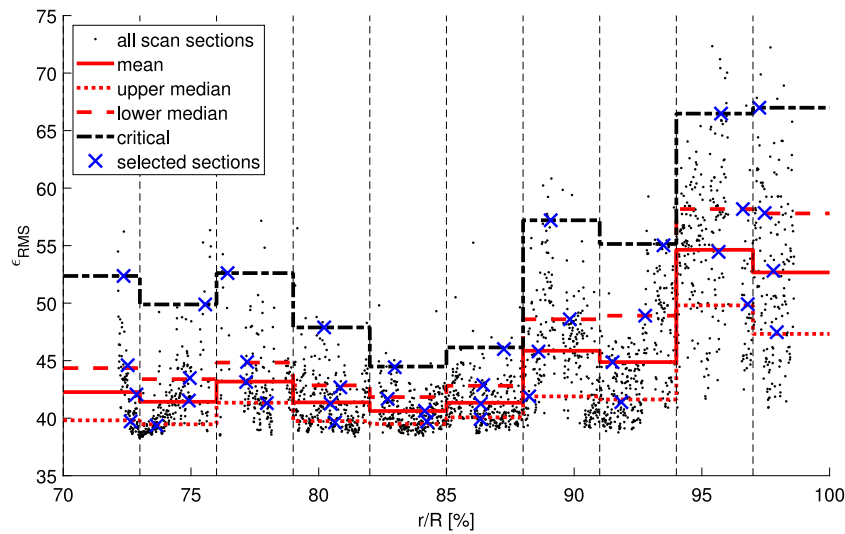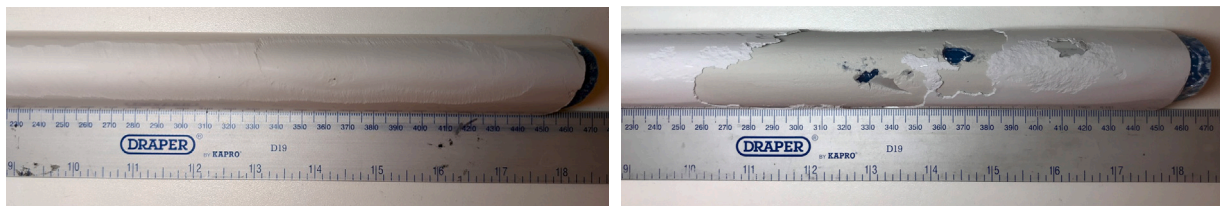
Fig. 3. Schematic of damaged airfoil selection criteria for defining four eroded blade models based on ε_{RMS} parameter. Black dots: values of ε_{RMS} of 2369 airfoils extracted from scan; red and black lines: ε_{RMS} levels of four damage states; blue 'X' marker: selected airfoils for four damage levels.

(a) Armour Edge thermoplastic erosion shield.

(b) Standard wind industry repair LEP system

Fig. 4. LEE geometry of two LEP systems tested to failure in R&D AS swirling arm rain erosion test facility of UK Offshore Renewable Energy Catapult. Courtesy of UK Offshore Renewable Energy Catapult.

of LEE geometries of the type shown in Fig. 4(b). Therefore, this geometry pattern is also included in the LEE analyses below, since it is representative of an observed LEE geometry type more irregular than that revealed by the laser scan. Two groove-shaped blade LEE geometries are added to the four LEE levels inferred from the scan. Both geometries assign to the groove of each of the ten strips values of s_u and s_l similar to those of the mean LE damage inferred from the scan. The two groove geometries differ from each other for the erosion depth d, set to the mean erosion depth obtained from the scan section for less severe erosion, and the maximum erosion depth of the same section for more severe erosion. The subplots of Fig. 5 depict the scan-based eroded LEs of the ten blade sections corresponding to the mean damage inferred by the scan, i.e. the airfoils marked with the 'X' symbol on the solid red line of Fig. 3. The figure also reports the two groove-shaped eroded LEs for each section, named 'd_{mean}-groove' and 'd_{max}-groove' hereafter. The left part of Table 1 provides the values of s_u, s_l, d_{mean} and d_{max} as percentages of the local chord for the ten blade sections of the mean damage inferred by the scan. For completeness, the middle and right parts also provide, respectively, the same parameters for the severe and mild damages.

3.3. Modeled roughness

A distributed roughness model is adopted to complete the scale separation analysis of the LEE damage. This model accounts for the impact of small irregular roughness not resolved by the laser scan on airfoil performance. As discussed in Section 2, the rough wall BL transition model of FLUENT requires both the geometric roughness height K and the equivalent sand grain roughness K_s, although its predictions depend predominantly on the value of K. For fully turbulent analyses, only the values of K_s is required.

The value of a probable scan resolution of 200 μm may be taken as an estimate of K for the unresolved roughness scales; thus, all modeled roughness analyses of this study assume $K = 200$ μm for the unresolved small roughness scales. The value of K_s depends on how the elements of the considered roughness topography interact with the BL [52,53]; available geometric correlations, relate K_s to both K and other geometric parameters of the roughness profile [27,54]. The ratio K_s/K can be larger or smaller than unity. For regular roughness patterns, it may range from 0.1 to 10 and above, depending on the shape and density of the roughness elements [27]. In the case of irregular roughness patterns, the ratio depends also on statistical properties of the roughness profile, and varies significantly among profiles with the same K [55]. Ref. [54] offers a comprehensive review of the correlations between K_s/K and the geometric parameters of roughness profiles.

Since the geometric parameters needed to calculate K_s/K are not known, the aerodynamic coefficients of all eroded airfoils for power and AEP loss calculations are computed parametrically, for K_s corresponding to a typical range of K_s/K. The chosen range $0.5 \le K_s/K \le 5$ corresponds to K_s varying from 100 to 1000 μm. The analysis of the sensitivity of airfoil aerodynamics and AEP losses to this parameter is presented in Section 4.

The modeled roughness is assumed to cover the LE from $x/c = 0$ to $x/c = 5.5\%$ on both sides of the eroded airfoil in all simulations, corresponding to $s_u/c = 7.6\%$ and $s_l/c = 6.8\%$ on the upper and lower sides, respectively. This range was used in previous studies [17,32], where a plausible extent of the LEE damage was estimated combining literature data and observation of photographs of damaged blades. In the case of groove-shaped LE erosion, the distributed roughness is applied over the groove surface and the two steps normal to the airfoil.
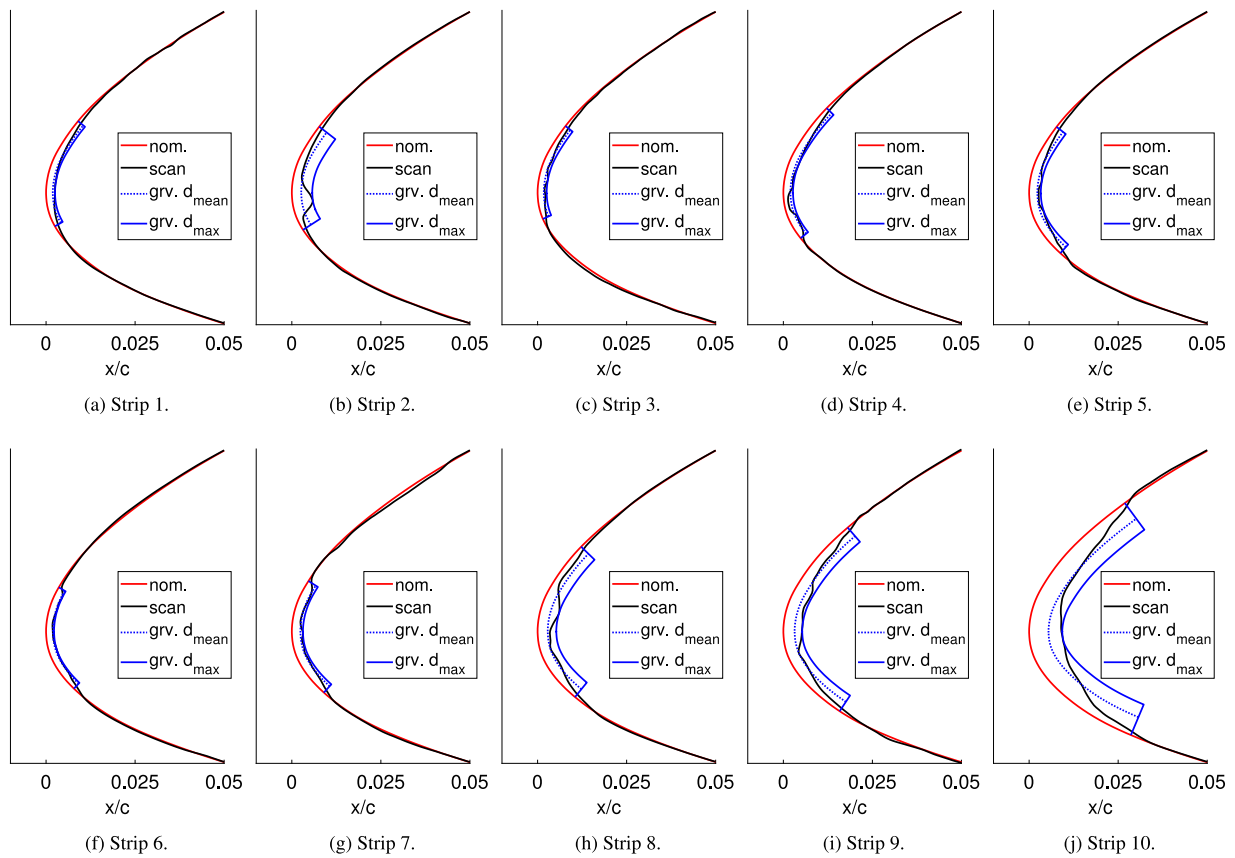
(a) Strip 1.   (b) Strip 2.   (c) Strip 3.   (d) Strip 4.   (e) Strip 5.

(f) Strip 6.   (g) Strip 7.   (h) Strip 8.   (i) Strip 9.   (j) Strip 10.

Fig. 5. Leading edge geometries of NACA63$_3$-618 airfoil: nominal geometry, mean scan-based erosion damage, and two groove-shaped damages with low and high erosion severity.

Table 1
Geometric parameters of mean, severe and mild scan-based LE damage of NACA63$_3$-618 airfoil.

Strip	Mean damage parameters (chord percentage)				Severe damage parameters (chord percentage)				Mild damage parameters (chord percentage)			
	s_l/c	s_u/c	d_{mean}/c	d_{max}/c	s_l/c	s_u/c	d_{mean}/c	d_{max}/c	s_l/c	s_u/c	d_{mean}/c	d_{max}/c
1	0.95	2.28	0.19	0.25	0.99	2.76	0.19	0.27	0.99	2.21	0.20	0.25
2	1.08	2.08	0.26	0.57	1.05	2.03	0.28	0.56	1.25	2.38	0.26	0.38
3	0.73	2.10	0.17	0.26	0.75	1.95	0.17	0.24	1.03	3.42	0.16	0.21
4	1.37	2.76	0.20	0.27	1.10	2.99	0.24	0.37	1.46	2.69	0.21	0.26
5	1.94	2.08	0.23	0.33	1.83	2.80	0.20	0.33	1.69	2.20	0.24	0.34
6	1.81	1.34	0.19	0.22	1.63	1.94	0.20	0.30	1.29	1.35	0.18	0.22
7	1.97	1.55	0.24	0.31	1.88	2.08	0.23	0.41	2.18	1.65	0.29	0.39
8	2.17	2.77	0.29	0.53	2.55	2.95	0.29	0.43	2.50	4.76	0.31	0.56
9	2.83	3.56	0.32	0.53	4.37	4.10	0.51	0.89	3.96	5.06	0.49	0.85
10	4.27	4.69	0.54	0.93	3.94	4.20	0.63	0.96	3.93	3.96	0.49	0.79

Most eroded airfoil simulations of this study assume that modeled small-scale roughness trip the BLs at the LE; thus, BLs are treated as fully turbulent from their onset. To verify this assumption, Figs. 6(a) and 6(b) compare, respectively, the $c_l(\alpha)$ curve and the drag polar of an eroded NACA63$_3$-618 airfoil computed using both the transitional and the fully turbulent analysis. The considered geometry is the blade section of strip 2 of the mean scan-based damage, centered at 74.5% rotor radius. The value $K = 200$ μm is used only by the transitional analysis, whereas $K_s = 100$ μm is used in both analyses. One observes that the $c_l(\alpha)$ curves and the drag polars obtained with the two simulations do not differ notably, confirming the validity of the fully turbulent BL assumption made above.

It is noted that the uncertainty on K_s is larger than that on K. However, numerical experiments, not reported for brevity, demonstrated that the position of the BL transition predicted by the rough wall $\gamma-Re_\theta$ SST transition model of FLUENT is fairly insensitive to the value of K_s, and is instead much more sensitive to the value of K. Other numerical tests also indicated that the fully turbulent and transitional

force coefficient curves remain very close to each other for $K > 200$ μm, as expected; the two curves start differing for K values well below the scan resolution of 200 μm.

3.4. Offshore and onshore sites

The AEP loss analyses are performed for two representative installation sites, one offshore and one onshore. The reference wind conditions of the offshore site are typical of a site in the North Sea. The mean annual wind speed at 90 m, the hub height of the considered offshore turbine, is 9.36 m/s; the shape factor of the Weibull distribution is 2. A power law with exponent 1/7 defines the vertical profile of the mean wind speed.

The reference wind conditions of the onshore site are taken from the Italian Wind Atlas [56]; they refer to a windy location in Southern Italy (41° 18′56″N, 15° 80′44′E). The mean annual wind speed at 100 m, the hub height of the considered onshore turbine, is 7.84 m/s, and the shape factor of the Weibull distribution is 1.88. The vertical wind
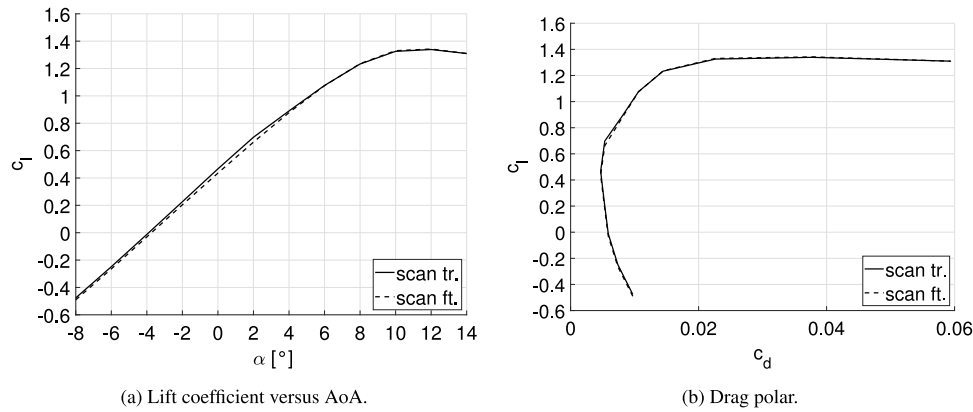
(a) Lift coefficient versus AoA.

(b) Drag polar.

Fig. 6. Force coefficients of eroded NACA63$_3$-618 airfoil at Re = 8.2M computed with transitional (tr.) and fully turbulent (ft.) simulations. Resolved erosion geometry is LEE of strip 2 of mean scan-based erosion, with modeled roughness defined by K = 200 µm and K_s = 100 µm. Values of K and K_s refer to real chord of strip.
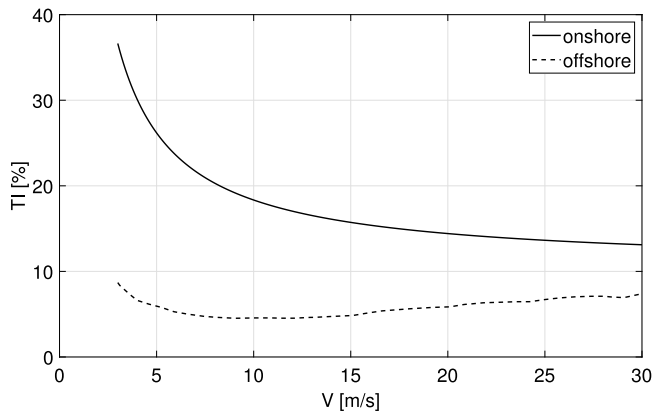

Fig. 7. Wind turbulent intensity at selected onshore and offshore sites.

profile is modeled by a power law with exponent 0.2. The hub height of the onshore turbine is greater than that of the offshore turbine to increase the energy capture, partly compensating for lower wind speeds at the hub height compared to offshore sites.

The wind TI also affects the turbine AEP due to the dependence of part of the power curve on this parameter [57]. The turbulent wind time series, used as input of OpenFAST to determine the mean power curve, are generated for each mean wind speed V and the corresponding TI level. For the onshore site, the TI(V) profile is based on the guidelines of the International Standard IEC61400. Assuming an onshore wind of class B, the TI for each wind speed is given by $TI = TI_{ref}(0.75 + 5.6/\bar{V})$ where TI_{ref} = 14%. Offshore TI is typically lower than onshore, and the formula above may lead to unrealistically high TI values. Therefore, the TI data for the offshore reference site are taken from the FINO 1 measurements [58,59], a dataset frequently used to characterize typical North Sea conditions. The measured TI levels were lower than 9%. The mean wind speed-dependent TI data of [59] have been used to generate the TurbSim wind time series for the offshore site. Fig. 7 reports the mean profiles TI(V) at the offshore and onshore sites. The notable TI level difference of the two sites has a significant weight on the difference between offshore and onshore AEP of a given turbine [7].

3.5. Mesh sensitivity and validation

The mesh topology used in this study is a structured C-grid. A MATLAB script generates the nominal and eroded airfoil geometries defined in Section 3.2, and runs the mesh generator ANSYS ICEM CFD version 19 - R3. The mesh sensitivity analysis below is performed by

comparing the force coefficients of the nominal NACA63$_3$-618 airfoil and the scan-based mildly eroded airfoil of strip 2 with distributed roughness defined by K_s = 200 µm. The simulation of the nominal smooth airfoil accounts for laminar-to-turbulent transition of the airfoil BLs using the $\gamma-Re_\theta$ SST transition model, whereas that of the eroded airfoil assumes fully turbulent BLs and uses the standard SST turbulence model. The AoA range is $-8° \leq \alpha \leq 14°$, using a step of 2°, and all simulations of the mesh sensitivity analysis use Re = 8.2M. Three grid levels are used. The coarse-, medium- and fine-refinement meshes have, respectively, 55 494, 126 940 and 284 916 cells; from coarse to fine, these grids use 422, 636 and 956 cells around the airfoil, and the minimum grid vertex-based wall distance of 2.7×10^{-6} chords yields $y^+ < 1$ in all simulations without rough wall functions. The aforementioned grid parameters apply to both nominal and eroded airfoil analyses.

Figs. 8(a) and 8(b) report, respectively, the lift curve and the drag polar of the nominal and eroded airfoils computed with the three aforementioned grids. In all cases the results of the three grids are very close to each other, and the medium and fine grid results are slightly closer than those of the coarse and medium grids are. Therefore, the medium-refinement mesh has been selected for all analyses of this study.

The CFD set-up used for this study has been successfully validated in several previous studies by comparing measured and computed force coefficients of different nominal and damaged variant counterparts. The clean DU96W-180 airfoil and a variant featuring severe LE grooves at Re = 1.5M, along with the nominal NACA64$_3$-618 airfoil at Re = 6M are examined in [22]; the clean DU96W-180 airfoil and a variant featuring LE erosion cavities and additional modeled roughness at Re = 1.5M are studied in [17]; the nominal NACA63$_3$-618 at Re = 9M is considered in [15]; the clean NACA63$_3$-418 and a variant featuring LE grooves with added modeled roughness at Re = 5M are studied in [5].

A new validation test, considering the wind tunnel experiments of [12] using the NACA63$_3$-418 airfoil at Re = 3.2M is considered below. The performance of the nominal airfoil with transitional BLs is compared to that of a variant with rough LE, with K_s = 101 µm per meter chord, roughness with density of 3% applied from the LE to x/c = 0.13 on the lower side and from the LE to x/c = 0.02 on the upper side. The roughness element height is K = 246 µm, and the choice of the ratio K_s/K yielding K_s = 101 is discussed in [12]. The CFD grid differs from the medium grid above only because it has 110,852 cells, 530 points along the airfoil, and minimum grid vertex-based wall distance of 7.2×10^{-6}. The constant a_1 of the SST model is set to 0.29. The clean airfoil analysis uses the $\gamma-Re_\theta$ SST transition model, whereas the rough LE analysis uses the fully turbulent SST model, since transition was observed to occur at the LE at most AoAs for this airfoil variant. Measured and computed data in Fig. 9 are in good agreement for both force coefficients, confirming the suitability of the developed CFD set-up for the investigations below.
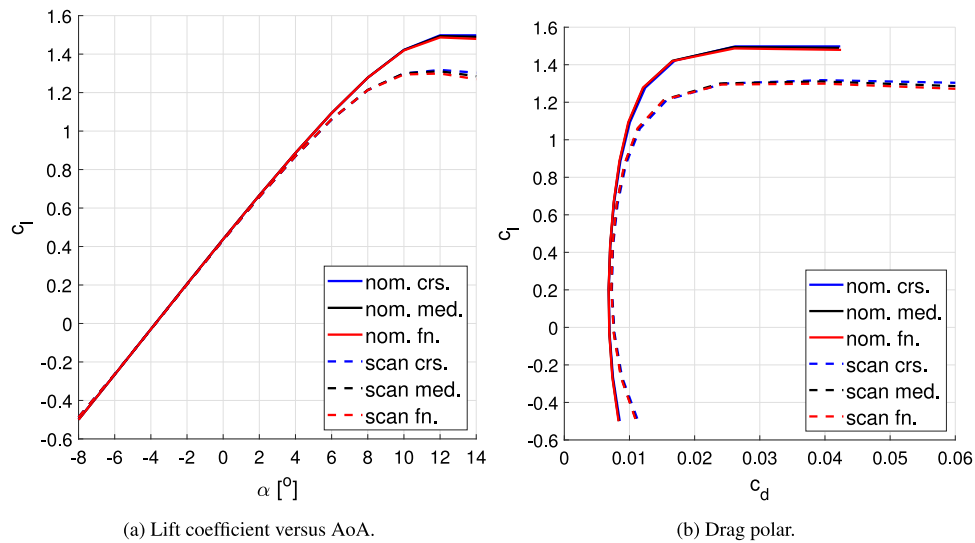
Fig. 8. Mesh sensitivity analysis of nominal and eroded NACA63$_3$-618 airfoils at Re = 8.2M. Resolved erosion geometry is LEE of strip 2 of mild scan-based erosion level, with modeled roughness defined by K_s = 200 μm.
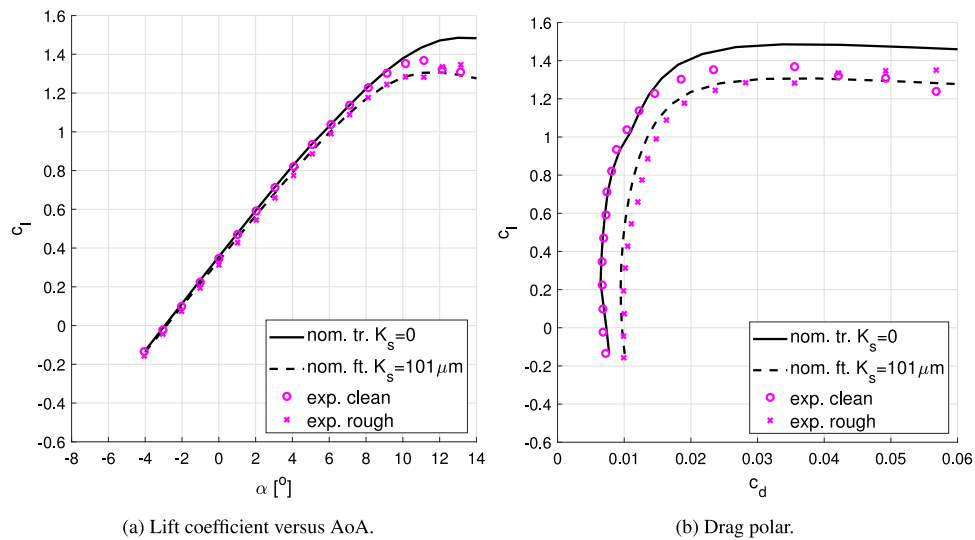

Fig. 9. Comparison of measured and computed force coefficients of nominal and rough-LE NACA63$_3$-418 airfoils at Re = 3.2M. Modeled roughness defined by K_s = 101 μm for meter chord.

4. Results

Fig. 10 compares the computed aerodynamic force coefficients of the nominal airfoil with free transition ('nom. tr.'), the nominal airfoil with transition forced at the LE ('nom. ft.'), one airfoil for mild, severe and critical scan-based damage ('scan mild', 'scan critical', and 'scan severe', respectively) and the d_{mean}-groove damage. The force coefficients of the four airfoils with resolved damage are those of strip 8, centered at 92.5% rotor radius. Figs. 10(a), 10(b) and 10(c) report, respectively, the $c_l(\alpha)$ curve, the drag polar and the aerodynamic efficiency ε of all indicated airfoils computed without distributed roughness ($K_s = 0$). Figs. 10(d), 10(e) and 10(f) report analyses similar to those of the first three subplots, but assume distributed roughness with $K_s = 200$ μm for the 'nom. ft.' and the four damaged airfoils, corresponding to $K_s/K = 1$; Figs. 10(g), 10(h) and 10(i) replicate the analyses of the first three subplots using a rough wall analysis with $K_s = 600$ μm, corresponding to $K_s/K = 3$. The indicated values of K_s refer to the real chord of the blade strip.

The analyses for $K_s = 200$ μm and $K_s = 600$ μm test the sensitivity of the computed performance to the value of K_s/K, an uncertain

parameter, for the assumed geometric roughness height $K = 200$ μm. They may be viewed also as testing the relative weight of modeled roughness scales on performance losses. The results of Fig. 10 indicate that the main reason for the aerodynamic performance impairment of the scan-based damaged sections is the loss of BL laminarity, since the largest difference between pairs of adjacent performance curves is that between the 'nom. tr.' and 'nom. ft.' curves for all considered K_s values. Moreover, as K_s increases, the force coefficient curves of the 'nom. ft.' and the scan-based damaged airfoils rapidly become very close to each other. The most notable performance variation of all damage variants is the reduction of their c_l as K_s increases. This indicates a weak dependence of the aerodynamic loss on the scan-based damage geometry and a larger dependence on K_s.

The trends above are inverted for the more localized damage of the airfoil with the d_{mean}-groove. Despite this geometry having the same mean depth $d/c = 0.0029$ of the severe scan-based damage, and the latter having a larger maximum depth of $d/c = 0.0045$ (Table 1), the groove-shaped damage yields a significantly larger impairment of the aerodynamic performance, which is also independent of K_s.
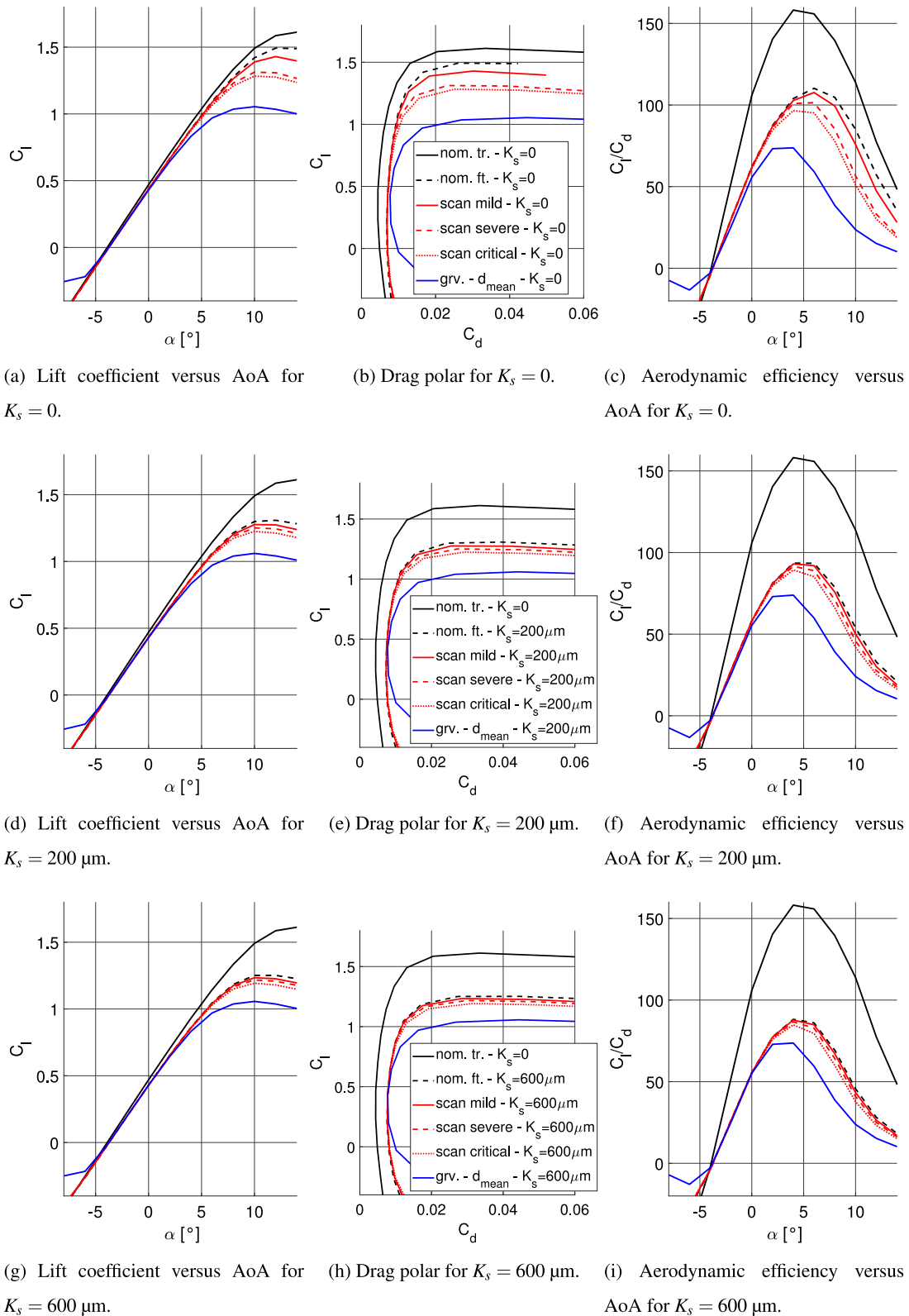
Fig. 10. Force coefficients of nominal and damaged NACA63$_3$-618 airfoils with scan-based erosion of strip 8 for different levels of equivalent sand grain roughness at Re = 8.2M. Values of K_s refer to real chord of strip.

The results above underline the importance of both resolving larger erosion scales, particularly for significantly jagged erosion geometries, and reliably estimating the equivalent sand grain roughness K_s.

Figs. 11(a) and 11(b) present the NREL 5 MW turbine AEP loss analysis based on the LE erosion geometries of the scan at the offshore and onshore site, respectively. The results of the ALPS analyses are clustered in sets of five damage states, and each set has a constant value of K_s. The first state is the 'nom. ft.' configuration, and the other four states use the resolved mild, mean, severe, and critical damages, i.e. the corresponding ten-airfoil sets defined in Section 3.2. In all cases,
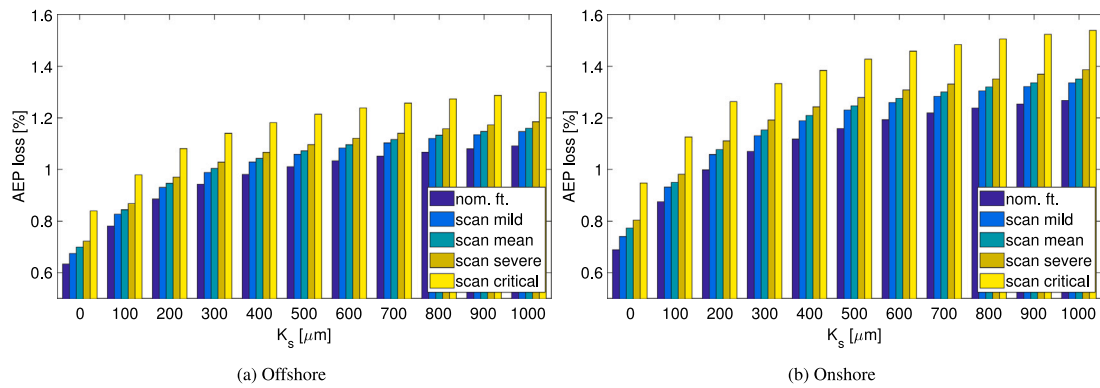
(a) Offshore
(b) Onshore

Fig. 11. AEP loss vs. K_s for nominal blade with forced transition (nom. ft.) and four damaged blades with mild, mean, severe and critical scan-based damages.

only damage over the outermost 30% of the blade is considered, and this blade portion is subdivided into ten strips positioned as indicated in Fig. 3. All five damage states are assessed for $K_s = 0$ and the ten K_s values defined in Section 3.3. Thus, 55 damaged variants of the reference turbine are examined; for each variant, all Reynolds number-dependent force coefficient curves needed by the OpenFAST/AeroDyn analysis are computed with CFD. For given K_s, each five-state histogram of Fig. 11 shows how the AEP loss evolves with severity of the resolved erosion. The variability among histograms, instead, indicates the AEP loss sensitivity to the uncertain sand grain roughness K_s of the unresolved roughness.

Since the laser scan resolution does not depend on the radial position along the blade, the value of K_s is kept constant in all CFD calculations of the force coefficients. However, the blade chord decreases from 3 m at 70% rotor radius to about 1.5 m at the blade tip. Therefore, for a set value of K_s/K, the ratio K_s/c, i.e. the value of K_s per meter chord, varies along the damaged blade portion.

As highlighted in Fig. 10, the relative differences of aerodynamic performance loss of the sections with resolved scan-based damage at $\alpha = 4.5°$, the mean AoA of the outermost 30% in region 2, are fairly independent of the modeled roughness parameter K_s. However, the performance of all sections with scan-based damage decreases by the same amount as K_s increases, or, equivalently, as K_s/K increases. These trends are reflected in the AEP loss analysis of Fig. 11. For given resolved damage, the AEP loss increases with K_s for $K_s < 500$ μm, and becomes fairly independent of this parameter for $K_s > 500$ μm. In the offshore case, for example, the AEP loss of the critical damage at $K_s = 0$ and $K_s = 500$ μm are 0.84% and 1.21%, respectively, whereas the loss is 1.30% at $K_s = 1000$ μm. The loss range of the resolved damages at $K_s = 1000$ μm is 0.21%, the difference between the loss of 1.30% of the critical damage and that of 1.09% of the 'nom. ft.' set-up. This difference does not vary significantly over the considered K_s range.

The trends highlighted above are also observed for the onshore installation, whose AEP losses are presented in Fig. 11(b). Comparing the AEP loss levels of Figs. 11(a) and 11(b) shows that, for a given damage variant, the onshore AEP loss is larger than the corresponding offshore loss. For example, at $K_s = 500$ μm the mean AEP loss of the five damaged variants is 1.09% at the offshore site and 1.27% at the offshore site. The higher AEP loss for given LE damage at onshore sites is due to both the lower yearly mean wind speeds and the higher turbulence intensity of these sites. An extensive study of the sensitivity of LEE-induced AEP losses to mean wind speed and turbulence intensity is reported in [5]. The sensitivity analyses of [7] also indicate that the AEP loss increase due to higher turbulence intensity at the onshore site may be comparable with that due to lower mean wind speed.

The impact of the two LE erosion grooves defined in Section 3.2 on AEP losses is examined in Fig. 12. Four damage variants are analyzed at six K_s values. The first two variants are the 'nom. ft' and the mean scan-based damage, reported for reference. The labels 'grv. d_{mean}' and 'grv.

d_{max}' refer to the d_{mean}-groove and d_{max}-groove LEE geometry, with the depths of the ten strips given, respectively, in the left and middle part of Table 1. The AEP loss of the groove-shaped LE damages, amounting to about 1.5% for the d_{mean}-groove and about 2% for the d_{max}-groove at the offshore site (Fig. 12(a)), is independent of K_s, unlike the loss of the two reference damages. Notably, despite the d_{mean}-groove damage having the same mean depth of the smoother mean scan-based damage, its AEP loss is always larger, up to twice as large at low K_s values. Similarly, the AEP loss of the d_{max}-groove damage, with depth equal to the maximum depth of the mean scan-based damage, is between two and more than three times that caused by the scan-resolved damage. The loss amplification arises because the localized perturbation to the LE smoothness given by the forward facing step on the upper side induces a strong local recirculation that severely weakens the BL. This impairs the airfoil overall performance over most positive AoAs, as visible in Fig. 10 and discussed further in [7,22]. This loss dominates over those of modeled or resolved smoother roughness, highlighting the strong dependence of the turbine performance reduction on the geometric characteristics of the larger resolved scales of erosion, which depend also on the LE material properties. The AEP loss trends at the onshore site (Fig. 12(b)) are the same of the offshore case.

LEE affects both the power, and the loads and controlled parameters of the turbine. The top left and right plots of Fig. 13 present, respectively, the percentage power loss of three damaged turbine variants at the offshore and onshore sites. The three variants are those with the 'nom. ft.', 'scan mean' and d_{mean}-groove blades, and $K_s = 500$ μm in all cases. The percentage power losses in Fig. 13 are computed dividing the difference between the damaged and nominal turbine of the time-averaged power at each mean wind speed by the nominal turbine power. This definition of the percentage variations applies to all results of the figure. In both offshore and onshore conditions, small power differences are observed between the nominal blade with fully turbulent BLs and that with mean resolved damage, consistently with the AEP loss analysis of Fig. 12. Power losses are notably higher for the d_{mean}-groove damage. In the offshore case, all three damage variants yield a large power loss near cut-in speed, and the d_{mean}-groove damage gives a fairly constant loss of about 3.4% in region 2 of the power curve. There is no power loss above the rated speed, since the pitch control reduces the blade pitch to compensate for the aerodynamic efficiency loss. The trends of the onshore power loss curves are similar. However, the largest power loss in region 2 is about 4.3%, and the damaged onshore turbines achieve the rated power at higher wind speed than their offshore counterparts, as observed also in [7].

The rotor thrust percentage variations of the offshore and onshore damaged turbine variants are shown in the left and right plots of the middle row of Fig. 13, respectively, whereas the percentage variations of the out-of-plane root bending moment are displayed in the bottom row of the figure. One sees that, when the blades feature a LE damage, both loads decrease before the rated wind speed. This is due primarily
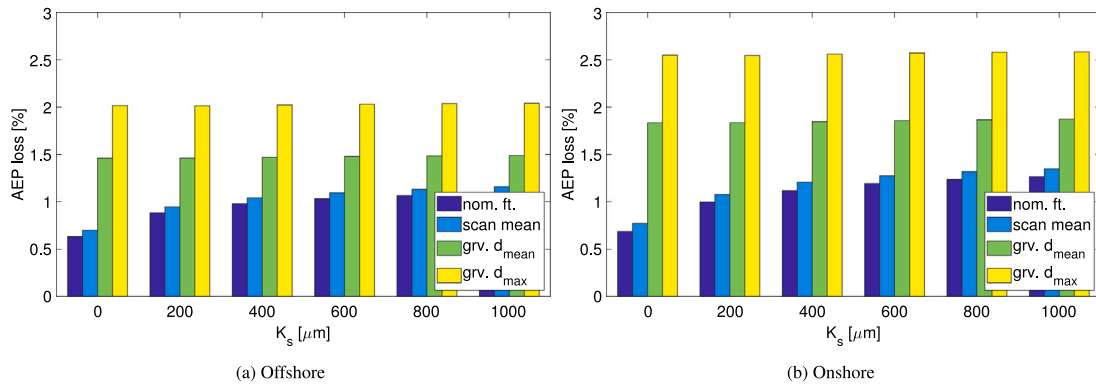
(a) Offshore　　　(b) Onshore

Fig. 12. AEP loss vs. K_s for nominal blade with forced transition (nom. ft.), damaged blade with mean scan-based damage, and damaged blades featuring two groove-shaped damages.
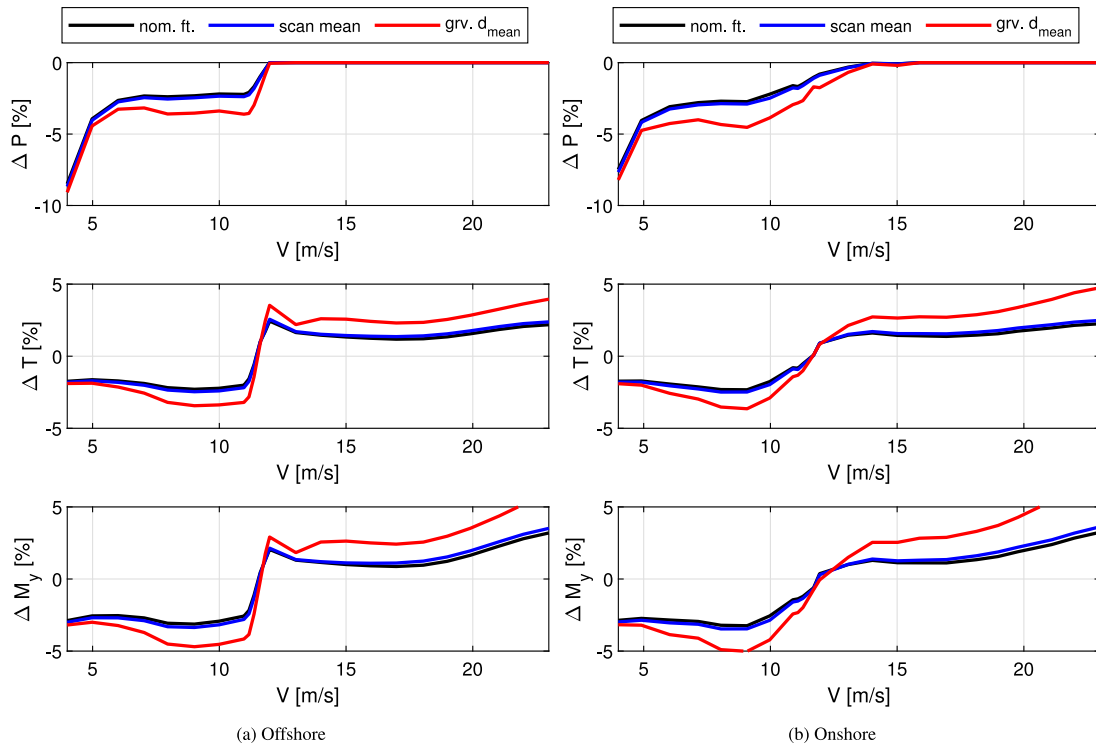

(a) Offshore　　　(b) Onshore

Fig. 13. Offshore (left) and onshore (right) percentage deviation from nominal values of power P, rotor thrust T, and out-of-plane root bending moment M_y for blade featuring nominal geometry and fully turbulent BLs, mean scan-based damage, and d_{mean}-groove damage ($K_s = 500$ μm).

to LEE-induced reductions of c_l. The lower lift coefficient yields a reduction of the lift force and its projection along the rotor axis, contributing to the observed reductions of rotor thrust and blade bending moment. Above the rated wind speed, the pitch control compensates for the reduced aerodynamic performance of the damaged blade by decreasing the blade pitch less than in the case of the nominal blade. This results in higher AoA at the eroded blade, enabling to increase the lift coefficient and the lift force. However, the lower pitch also results in a larger force projection along the rotor axis, increasing rotor thrust and blade bending moment. As for the power, the load variations of the groove-shaped damage are larger than those of the other two LEE states. The percentage load variations for given LE damage at the offshore and onshore sites are comparable.

The top left and right plots of Fig. 14 show the rotor speed variation of the three damaged turbine variants with respect to the reference turbine at the offshore and onshore sites, respectively. The magnitude of the observed negative variations is very small. It is interesting noting that the rotor speed of turbines with LE damage was observed to

increase when using the so-called adaptive turbine control for eroded rotors proposed in Campobasso et al. [22]. The adaptive control updates the original tip-speed-ratio λ of the nominal turbine, replacing it with the λ value yielding the maximum power coefficient of the turbine with LEE.

The bottom left and right plots of Fig. 14 depict the blade pitch variation of the three damaged turbine variants with respect to the reference turbine at the offshore and onshore sites, respectively. The variation above rated wind speed is negative, indicative that the pitch angle of the eroded blades is smaller than that of the nominal blades. As expected, the turbine with the largest damage is that with the largest pitch reduction, since the aerodynamic performance reduction is largest.

5. Conclusions

A RANS CFD- and BEMT-based investigation into the progression of offshore and onshore wind turbine AEP losses corresponding to
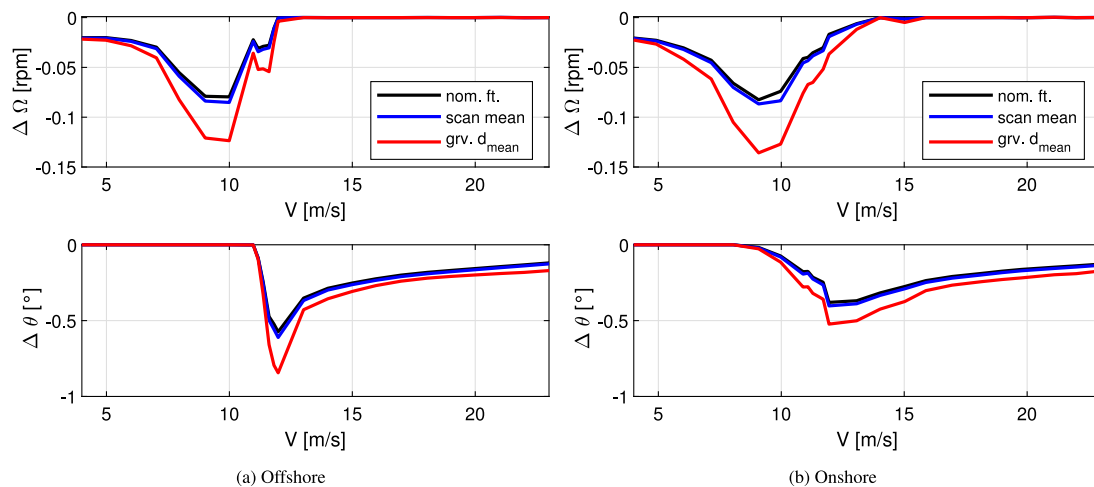
Fig. 14. Offshore (left) and onshore (right) deviation from nominal values of rotor speed Ω, and blade pitch θ for blade featuring nominal geometry and fully turbulent BLs, mean scan-based damage, and d_{mean}-groove damage ($K_s = 500$ μm).

the progression of blade LEE has been presented. Two eroded LE topographies have been considered. One is typical of materials that erode fairly smoothly, without severe localized geometry irregularities, with four erosion stages of increasing severity inferred from the laser scan of the eroded LE of an offshore turbine; the other topography type, observed in rain erosion test photographs and also reported in the literature, refers to materials that erode more irregularly, with patterns resembling chordwise LE grooves.

The adopted scale separation analysis of LEE aerodynamics, that resolves erosion scales detectable with laser scans and models the effects of unresolved small scales with a K_s-based distributed roughness model, shows that (a) the AEP loss variability due to varying degrees of smooth resolved erosion is smaller than the loss variability with K_s, and (b) localized geometric irregularities of the LE geometry yield larger AEP losses than smoother erosion with comparable depth, and are insensitive to K_s. These conclusions emphasize the necessity of resolving large scale erosion and developing a LE material-focused geometric roughness database needed to estimate the equivalent sand grain roughness K_s, thus reducing its uncertainty in LEE RANS analyses.

At the considered offshore site, the largest AEP loss, caused by localized groove-shaped irregularities, amounts to about 2%. For smoother large-scale erosion, AEP losses reach about 1.3% at large K_s values. For a plausible variability range $0.5 < K_s/K < 2.5$, the AEP loss of the turbine with nominal airfoils and small-scale distributed roughness varies between about 0.78 and 1.09%.

The onshore AEP loss trends are similar to those at the offshore site. However, losses are larger, due to both lower mean wind speed and higher TI. The AEP loss due to the most severe groove-shaped LE damage is about 2.5%. Moreover, the variability of K_s/K results in larger variability of the AEP loss than at the offshore site. For example, $0.5 < K_s/K < 2.5$ results in the AEP loss of the turbine with nominal blade geometry and roughened LEs varying between about 0.88 and 1.27%.

The effects of LEE on the variations of rotor loads and control parameters from cut-in to cut-out speeds have also been assessed. The most notable effects of LEE are the reduction of rotor thrust and root bending moment between cut-in and rated wind speeds, and their increase above rated wind speed, due to reduced blade pitch angles to maintain the rated power despite the reduced aerodynamic efficiency of the blades. As reported in previous studies, the power and AEP loss before the rated power is achieved may be alleviated by implementing an adaptive control strategy [22].

The performance analysis of the resolved scan-based LEE damage may be affected by yet undefined uncertainty due to the adopted 2D CFD approach. Based on preliminary investigations, however, these analyses will require new validation data based on wind tunnel testing and simulation technologies with higher fidelity than RANS CFD.

CRediT authorship contribution statement

Alessio Castorrini: Data curation, Formal analysis, Investigation, Methodology, Supervision, Validation, Visualization, Writing – original draft. **Andrea Ortolani:** Data curation, Investigation, Methodology, Validation, Visualization. **M. Sergio Campobasso:** Conceptualization, Formal analysis, Funding acquisition, Investigation, Methodology, Project administration, Resources, Supervision, Writing – original draft, Writing – review & editing.

Declaration of competing interest

The authors declare that they have no known competing financial interests or personal relationships that could have appeared to influence the work reported in this paper.

References

[1] European commission. European green deal, 2019, , Accessed on February 18, 2023.

[2] IRENA, Renewable Power Generation Costs in 2021, Technical report, IRENA, 2022.

[3] W. Han, J. Kim, B. Kim, Effects of contamination and erosion at the leading edge of blade tip airfoils on the annual energy production of wind turbines, Renew. Energy 115 (2018) 817–823.

[4] H. Law, V. Koutsos, Leading edge erosion of wind turbines: Effect of solid airborne particles and rain on operational wind farms, Wind Energy 23 (2020) 1955–1965.

[5] L. Cappugi, A. Castorrini, A. Bonfiglioli, E. Minisci, M.S. Campobasso, Machine learning-enabled prediction of wind turbine energy yield losses due to general blade leading edge erosion, Energy Convers. Manage. 245 (2021) 114567.

[6] K. Panthi, G.V. Iungo, Quantification of wind turbine energy loss due to leading-edge erosion through infrared-camera imaging, numerical simulations, and assessment against SCADA and meteorological data, Wind Energy 26 (2023) 266–282.

[7] M.S. Campobasso, A. Castorrini, A. Ortolani, E. Minisci, Probabilistic analysis of wind turbine performance degradation due to blade erosion accounting for uncertainty of damage geometry, Renew. Sustain. Energy Rev. 178 (2023) 113254.

[8] K. Gharali, D.A. Johnson, Numerical modeling of an S809 airfoil under dynamic stall, erosion and high reduced frequencies, Appl. Energy 93 (2012) 45–52, (1) Green Energy; (2) Special Section from papers presented at the 2nd International Enery 2030 Conf..

[9] R.P.J.O.M. van Rooij, W.A. Timmer, Roughness sensitivity considerations for thick rotor blade airfoils, J. Solar Energy Eng. 125 (2003) 468–478.

[10] D.M. Somers, J.L. Tangler, Wind tunnel test of the S814 thick root airfoil, J. Solar Energy Eng. 118 (1996) 217–221.

[11] D.C. Maniaci, E.B. White, B. Wilcox, C.M. Langel, C. van Dam, J.A. Paquette, Experimental measurement and CFD model development of thick wind turbine airfoils with leading edge erosion, J. Phys. Conf. Ser. 753 (2016) 022013.

[12] C. Langel, M. Chow, C. Van Dam, D. Maniaci, RANS Based Methodology for Predicting the Influence of Leading Edge Erosion on Airfoil Performance, Technical Report SAND2017-11289,, Langley Aeronautical Laboratory, Albuquerque, New Mexico and Livermore, California, 2017.

[13] P.K. Kundu, I.M. Cohen, D.R. Dowling, Fluid Mechanics, Academic Press, 2015.

[14] A.L. Braslow, E.C. Knox, Simplified Method for Determination of Critical Height of Distributed Roughness Particles for Boundary-Layer Transition At Mach Numbers from 0 To 5, Technical Report 4363, Langley Aeronautical Laboratory, Langley Field, VA, USA, 1958.

[15] A. Ortolani, A. Castorrini, M.S. Campobasso, Multi-scale Navier–Stokes analysis of geometrically resolved erosion of wind turbine blade leading edges, J. Phys. Conf. Ser. 2265 (2022) 032102.

[16] F. Ghanadi, L. Djenidi, Study of a rough-wall turbulent boundary layer under pressure gradient, J. Fluid Mech. 938 (2022) A17.

[17] M. Campobasso, A. Castorrini, L. Cappugi, A. Bonfiglioli, Experimentally validated three-dimensional computational aerodynamics of wind turbine blade sections featuring leading edge erosion cavities, Wind Energy 25 (2022) 168–189.

[18] Y. Liu, M. Hajj, Y. Bao, Review of robot-based damage assessment for offshore wind turbines, Renew. Sustain. Energy Rev. 158 (2022) 112187.

[19] A. Shihavuddin, X. Chen, V. Fedorov, A. Nymark Christensen, N. Andre Brogaard Riis, K. Branner, A. Bjorholm Dahl, R. Reinhold Paulsen, Wind turbine surface damage detection by deep learning aided drone inspection analysis, Energies 12 (2019).

[20] P. Durdevic, D. Ortiz Arroyo, Z. Yang, Lidar assisted camera inspection of wind turbines - experimental study, in: 2019, 1st International Conference on Electrical, Control and Instrumentation Engineering (ICECIE), Aalborg, Denmark.

[21] M. Car, L. Markovic, A. Ivanovic, M. Orsag, S. Bogdan, Autonomous wind-turbine blade inspection using lidar-equipped unmanned aerial vehicle, IEEE Access 8 (2020) 131380–131387.

[22] M. Campobasso, A. Cavazzini, E. Minisci, Rapid estimate of wind turbine energy loss due to blade leading edge delamination using artificial neural networks, J. Turbomach. 142 (2020).

[23] E. Krog Kruse, C. Bak, A.S. Olsen, Wind tunnel experiments on a NACA 633-418 airfoil with different types of leading edge roughness, Wind Energy 24 (2021) 1263–1274.

[24] N. Gaudern, A practical study of the aerodynamic impact of wind turbine blade leading edge erosion, J. Phys. Conf. Ser. 524 (2014) 012031.

[25] A. Sareen, C.A. Sapre, M.S. Selig, Effects of leading edge erosion on wind turbine blade performance, Wind Energy 17 (2014) 1531–1542.

[26] A. Koodly Ravishankara, H. Ã-zdemir, E. van der Weide, Analysis of leading edge erosion effects on turbulent flow over airfoils, Renew. Energy 172 (2021) 765–779.

[27] J. Jiménez, Turbulent flows over rough walls, Annu. Rev. Fluid Mech. 36 (2004) 173–196.

[28] K.A. Flack, M.P. Schultz, J.S. Connelly, Examination of a critical roughness height for outer layer similarity, Phys. Fluids 19 (2007) 095104.

[29] M. Schramm, H. Rahimi, B. Stoevesandt, K. Tangager, The influence of eroded blades on wind turbine performance using numerical simulations, Energies 10 (2017).

[30] F. Papi, F. Balduzzi, G. Ferrara, A. Bianchini, Uncertainty quantification on the effects of rain-induced erosion on annual energy production and performance of a multi-mw wind turbine, Renew. Energy 165 (2021) 701–715.

[31] Y. Wang, R. Hu, X. Zheng, Aerodynamic analysis of an airfoil with leading edge pitting erosion, J. Solar Energy Eng. 139 (2017) 061002.

[32] A. Castorrini, L. Cappugi, A. Bonfiglioli, M. Campobasso, Assessing wind turbine energy losses due to blade leading edge erosion cavities with parametric CAD and 3D CFD, J. Phys. Conf. Ser. 1618 (2020) 052015.

[33] K. Vimalakanthan, H. van der Mijle Meijer, I. Bakhmet, G. Schepers, Computational fluid dynamics (CFD) modeling of actual eroded wind turbine blades, Wind Energy Sci. 8 (2023) 41–69.

[34] J. Jonkman, M. Sprague, OpenFAST: An Aeroelastic Computer-Aided Engineering Tool for Horizontal Axis Wind Turbines, National Renewable Energy Laboratiry, Golden, Colorado, nwtc.nrel.gov/OpenFAST, accessed on 10 2023.

[35] G. Heyman, B. Jonkman, R. Murray, R. Damiani, J. Jonkman, AERODYN: a time-domain wind and MHK turbine aerodynamics module, 2021, , Accessed on 5 2021.

[36] M. Hansen, Aerodynamics of Wind Turbines, Routledge, 2015.

[37] R.R. Damiani, G. Hayman, The Unsteady Aerodynamics Module for FAST 8, Technical report, National Renewable Energy Lab.(NREL, Golden, CO (United States), 2019.

[38] J. Jonkman, S. Butterfield, W. Musial, G. Scott, Definition of a 5-MW Reference Wind Turbine for Offshore System Development, Technical Report NREL/TP-500-38060, NREL, Golden, CO, USA, 2009.

[39] B.J. Jonkman, Turbsim User's Guide: Version 1.50, Technical report, National Renewable Energy Lab.(NREL, Golden, CO (United States), 2009.

[40] J.C. Kaimal, J.C. Wyngaard, Y. Izumi, O.R. CotÃ, Spectral characteristics of surface-layer turbulence, Q. J. R. Meteorol. Soc. 98 (1972) 563–589.

[41] Ansys-Inc, Fluent theory guide, release 2019.r3, 2023, www.ansys.com/Products/Fluids/ANSYS-Fluent, 2019, Accessed on 10 2023.

[42] F. Menter, Two-equation turbulence-models for engineering applications, AIAA J. 32 (1994) 1598–1605.

[43] F. Menter, R. Langtry, S. Likki, Y. Suzen, P. Huang, S. VÃlker, A correlation-based transition model using local variables â part I: Model formulation, J. Turbomach. 128 (2006) 413–422.

[44] R. Langtry, F. Menter, S. Likki, Y. Suzen, P. Huang, S. VÃlker, A correlation-based transition model using local variables â part II: Test cases and industrial applications, J. Turbomach. 128 (2006) 423–434.

[45] R. Langtry, F. Menter, Correlation-based transition modeling for unstructured parallelized computational fluid dynamics codes, AIAA J. 47 (2009) 2894.

[46] M. Kato, B. Launder, The modelling of turbulent flow around stationary and vibrating square cylinders, in: Paper (1993) 10-4, 9th Symposium on Turbulent Shear Flows, Kyoto, Japan, 1993.

[47] B. Launder, D. Spalding, The numerical computation of turbulent flows, Comput. Methods Appl. Mech. Engrg. 3 (1974) 269–289.

[48] L.A. Viterna, D.C. Janetzke, Theoretical and Experimental Power from Large Horizontal-Axis Wind Turbines, Technical report, National Aeronautics and Space Administration, Lewis Research Center, Cleveland, OH, 1982.

[49] S.A. Ning, Airfoilprep.py: A python module for preprocessing aerodynamic airfoil data primarily for wind turbine applications, 2023, , Accessed on 25 2023.

[50] Lancaster University, High end computing (HEC), 2023, www.lancaster.ac.uk/iss/info/ITh{and}outs/hec/HEC-flyer.pdf, Accessed on 1 2023.

[51] A. Meyer Forsting, A.S. Olsen, N.N. Sø rensen, C. Bak, The impact of leading edge damage and repair on sectional aerodynamic performance, in: AIAA Paper (2023) 2023-0968, AIAA SCITECH 2023 Forum, National Harbor, Maryland, 2023.

[52] H. Schlichting, Experimentelle Untersuchungen zum Rauhigkeitsproblem, Ing.-Arch. 7 (1936) 1–34.

[53] A. Busse, O. Zhdanov, Direct numerical simulations of turbulent channel flow over ratchet roughness, Flow Turbul. Combust. 109 (2022) 1195–1213.

[54] M. Kadivar, D. Tormey, G. McGranaghan, A review on turbulent flow over rough surfaces: Fundamentals and theories, Int. J. Thermofluids 10 (2021) 100077.

[55] M. Thakkar, A. Busse, N. Sandham, Surface correlations of hydrodynamic drag for transitionally rough engineering surfaces, J. Turbul. 18 (2017) 138–169.

[56] Atlas eolico, 2022, , Milan, Italy. Accessed: 2022-10-31.

[57] L.M. Bardal, L.R. SÃtran, Influence of turbulence intensity on wind turbine power curves, Energy Procedia 137 (2017) 553–558, 14th Deep Sea Offshore Wind R & D Conference, EERA DeepWind'2017.

[58] E. Berge, Ø. Byrkjedal, Y.W. Ydersbond, D. Kindler, Modelling of offshore wind resources. Comparison of a mesoscale model and measurements from FINO 1 and north sea oil rigs, in: European Wind Energy Conference, 2009.

[59] S. Emeis, Current issues in wind energy meteorology, Meteorol. Appl. 21 (2014) 803–819.